

1

2

3

## Coarse-grained simulations of actomyosin rings point to a nodeless model

4

### involving both unipolar and bipolar myosins

5

*Lam T. Nguyen<sup>a,b</sup>, Matthew T. Swulius<sup>a,b</sup>, Samya Aich<sup>c</sup>, Mithilesh Mishra<sup>c</sup>, Grant J. Jensen<sup>a,b,1</sup>*

6

*<sup>a</sup> California Institute of Technology, Pasadena, CA 91125*

7

*<sup>b</sup> Howard Hughes Medical Institute*

8

*<sup>c</sup> Tata Institute of Fundamental Research, India*

9

*<sup>1</sup> To whom correspondence should be addressed: [jensen@caltech.edu](mailto:jensen@caltech.edu), (626) 395 8827*

10

11

12

13

14

**Keywords:** coarse-grained simulations, cell division, cytokinesis, actomyosin ring, molecular dynamics

## 15 **Abstract**

16 Cytokinesis in most eukaryotic cells is orchestrated by a contractile actomyosin ring. While many of the  
17 proteins involved are known, the mechanism of constriction remains unclear. Informed by existing literature  
18 and new 3D molecular details from electron cryotomography, here we develop 3D coarse-grained models of  
19 actin filaments, unipolar and bipolar myosins, actin crosslinkers, and membranes and simulate their  
20 interactions. Exploring a matrix of possible actomyosin configurations suggested that node-based architectures  
21 like those presently described for ring assembly result in membrane puckers not seen in EM images of real  
22 cells. Instead, the model that best matches data from fluorescence microscopy, electron cryotomography, and  
23 biochemical experiments is one in which actin filaments transmit force to the membrane through evenly-  
24 distributed, membrane-attached, unipolar myosins, with bipolar myosins in the ring driving contraction. While  
25 at this point this model is only favored (not proven), the work highlights the power of coarse-grained  
26 biophysical simulations to compare complex mechanistic hypotheses.

27

28

29

30

31 **Significance Statement**

32 In most eukaryotes, a ring of actin and myosin drives cell division, but how the elements of the ring are  
33 arranged and constrict remain unclear. Here we use 3D coarse-grained simulations to explore various  
34 possibilities. Our simulations suggest that if actomyosin is arranged in nodes (as suggested by a popular model  
35 of ring assembly), the membrane distorts in ways not seen experimentally. Instead, actin and myosin are more  
36 likely uniformly distributed around the ring. In the model that best fits experimental data, ring tension is  
37 generated by interactions between bipolar myosins and actin, and transmitted to the membrane via unipolar  
38 myosins. Technologically the study highlights how coarse-grained simulations can test specific mechanistic  
39 hypotheses by comparing their predicted outcomes to experimental results.

40

41

## 42 **Introduction**

43 It is well known that an actomyosin ring (AMR) drives cell division in most eukaryotic cells, but how it  
44 contracts and how force is transmitted to the membrane remain unclear (1, 2). Two components involved in  
45 contraction are actin filaments (F-actin) and the motor protein, non-muscle myosin II, which exerts tensile  
46 force on F-actin through a processive ATP-dependent power stroke mechanism (3). Both proteins are essential  
47 for cytokinesis and localize to an equatorial contractile ring during mitosis (4–12). Fluorescence studies of  
48 ring assembly in *Schizosaccharomyces pombe*, a rod-shaped unicellular fission yeast that shares most of the  
49 cytokinesis genes with metazoans (1), showed that the ring components first form a broad band of nodes (13,  
50 14) that coalesce into a ring at the division plane (15). Recent electron cryotomography (ECT) of dividing  
51 fission yeast showed, however, that F-actin termini are apparently randomly distributed around the ring (16),  
52 calling into question whether nodes continue to exist during constriction. F-actin in the contractile ring is  
53 contributed by both existing actin cables (17) and de novo nucleation, primarily by the formin Cdc12p (18), a  
54 barbed-end actin-capping dimeric protein that is essential for ring assembly in fission yeast (19). While it has  
55 been proposed that ring tension is transmitted to the membrane via connection between the actin barbed end  
56 and Cdc12p, which either exists individually (2) or at nodes (20), this mechanism has not been proven.

57

58 There are two myosin type-II heavy chains (Myo2p and Myp2p) in the contractile ring. Myo2p, the essential  
59 type II myosin (6, 21), plays the leading role in ring assembly while the second, non-essential, unconventional  
60 type II myosin, Myp2p, is the major driver for ring constriction (22), consistent with its arrival at the division  
61 site immediately prior to ring constriction (12). Recent evidence indicates that during constriction, Myo2p and  
62 Myp2p are distributed in two distinct concentric rings (22), but the causes and functional implications of this  
63 segregation are unknown. While previous simulation studies have described myosin as bipolar (23, 24), and  
64 this assumption is supported by some *in vitro* evidence (25, 26), myosin has also been proposed to exist in a  
65 unipolar form with its C-terminal tail tethered to the membrane and its N-terminal motor domain in the

66 cytoplasm, in a ‘bouquet-like’ arrangement (20, 27). Further study is needed to elucidate how myosin is  
67 organized within the ring and how it generates tension during constriction.  
68  
69 In addition to F-actin and myosin, the actin crosslinkers  $\alpha$ -actinin and fimbrin have been reported to be  
70 important for assembly of the ring (28, 29). While  $\alpha$ -actinin is present in the ring during constriction, it is not  
71 clear whether fimbrin is present as well (30). In vitro, however, addition of actin-crosslinkers stalls ring  
72 contraction (31). Thus it is presently unclear how these actin crosslinkers affect ring contraction. Cofilin has  
73 also been reported to help maintain the structure of the ring, but its seemingly counterintuitive function as an  
74 F-actin severing protein (32, 33) leaves its role during ring constriction unclear.  
75  
76 Simulations have been used previously to explore constriction of the actomyosin ring (34). In an early  
77 continuum model, discrete molecules were not described. Instead the ring was represented by density values  
78 and the roles of myosin and crosslinkers were implicitly represented using coefficients of tension contribution  
79 (35). Simulations based on this model suggested that actin depolymerization in the presence of end-tracking  
80 crosslinkers could drive constriction, but whether such a crosslinker exists is unknown. Later simulations  
81 further explored this same idea, modeling individual filaments as lines with defined polarity (36). In more  
82 recent work, the ring was modeled as a 2D band in which actin filaments were modeled as chains of beads and  
83 clusters of myosins were represented as single beads which exerted force on actin filaments in close proximity  
84 (24). Parameters were found in which this 2D model produced tension similar to that measured in fission yeast  
85 protoplasts. Simulations have also explored the condensation of the ring before constriction (37).  
86  
87 Prompted by new electron cryotomography (ECT) data revealing for the first time the native 3D organization  
88 of the actin filaments and the membrane in dividing yeast cells (16), here we developed more detailed and 3D  
89 coarse-grained simulations to explore different hypotheses about how actin and myosin might constrict the  
90 membrane. F-actin, unipolar and bipolar myosins, and actin crosslinkers were all modeled using a bead-spring

91 representation. A flexible cylindrical membrane was also modeled. To make actomyosin interactions as  
92 realistic as possible, the ATPase cycle of myosin was implemented in step-by-step detail. Random forces were  
93 further added to mimic thermal fluctuation.

94

95 First, we introduced the basic components of the ring one-by-one to define a minimal set of components and  
96 rules necessary for constriction. In doing so, we found that actin crosslinkers are required to propagate tension  
97 through the ring, and that introducing cofilin to sever bent F-actin helps reproduce the filament straightness  
98 observed by ECT. We then explored sixteen candidate actomyosin architectures and ring-to-membrane  
99 attachments. Combined with ECT data, our results suggest that actomyosin does not exist in nodes during  
100 constriction. Judged by all currently available experimental data, our simulations favor a model in which the  
101 ring tension is generated primarily through interactions between bipolar myosins and actin filaments, and is  
102 transmitted to the membrane via unipolar myosins, which are individually attached to the membrane. Due to  
103 the 3D and dynamic nature of our data, which is much better presented in movies than static figures, we  
104 encourage readers to begin by watching [Movie S1](#), which presents (i) the elements and properties of our 3D  
105 coarse-grained model of the contractile ring, (ii) building the initial model, (iii) exploration of different  
106 actomyosin configurations, and (iv) a final model that best agreed with experimental data.

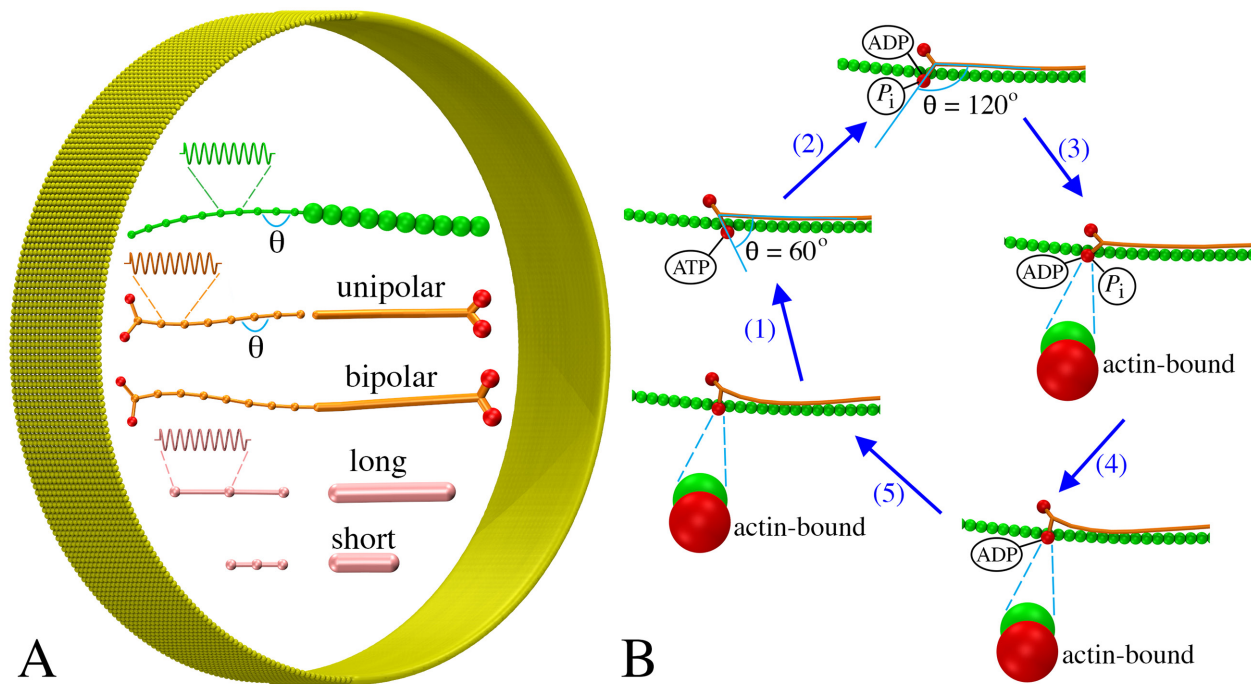
## 107 **Results**

### 108 **Basic components of the ring**

109 To build a coarse-grained model of the contractile ring, three main components of the ring including F-actin,  
110 myosin and crosslinkers were represented using a bead-spring model (Fig. 1A). Each filament was modeled as  
111 a chain of beads connected by springs, each myosin was modeled to be either unipolar or biopolar, and each  
112 crosslinker was modeled to have two actin binding domains at the two ends. The membrane was modeled as a  
113 sheet of beads, originally having a cylindrical shape (Fig. 1A). Actin-myosin interaction was modeled to occur  
114 in a power-stroke fashion in which the myosin ATPase cycle had five steps (Fig. 1B). The power stroke was  
115 generated via changing the angle of the myosin head as it transitioned between its ATPase phases (see  
116 [Methods for details](#)).

117  
118 Many proteins are present at the mid-cell during constriction, but it is unclear which are essential for the  
119 contractility of the ring. We therefore started with a very simple model, testing interactions between bipolar  
120 myosin and F-actin of mixed polarities, originally arranged into a ring ([Methods/Initial ring configuration](#)).  
121 In this test, a membrane was added to confine the actomyosin system, but membrane constriction was not  
122 expected since it was not linked to the ring (Fig. 2A). As myosin moved along F-actin toward their plus ends  
123 in a ATPase-dependent power-stroke fashion (Fig. 1B), the filaments slid, bent and oriented randomly, but the  
124 ring did not constrict due to the lack of long-range propagation of tension around the ring (Fig. 2B; [Movie S1, at 2:10](#)). Reasoning that crosslinking F-actin would help propagate tension, actin crosslinkers were added, and  
125 the ring began to contract, despite losing the original ring-like arrangement of F-actin (Fig. 2C; [Movie S1, at 2:35](#)). Linking the ring to the membrane ([Methods/Membrane tethering](#)) resulted in membrane constriction  
126 showing that a ring composed of F-actin, myosin and actin crosslinkers is capable of generating tension and  
127 constricting the membrane (Fig. 2D; [Movie S1, at 3:01](#)). As the membrane was pulled inward, cell wall  
128 material was added behind preventing the membrane from relaxing back (see [Methods](#)). The ring-like  
129 arrangement of F-actin was now maintained, suggesting that membrane attachment contributes to maintenance  
130  
131

132 of the ring structure. Note that in later simulations of model 1, tethering the actin plus end and unipolar  
133 myosin tail to membrane-bound nodes produced tension temporarily in the absence of crosslinkers. As the  
134 nodes were able to slide on the membrane to aggregate into separated large clusters, however, the ring was  
135 quickly broken (SI Appendix/Fig. S2A), pointing again to the need of crosslinkers for ring constriction.  
136



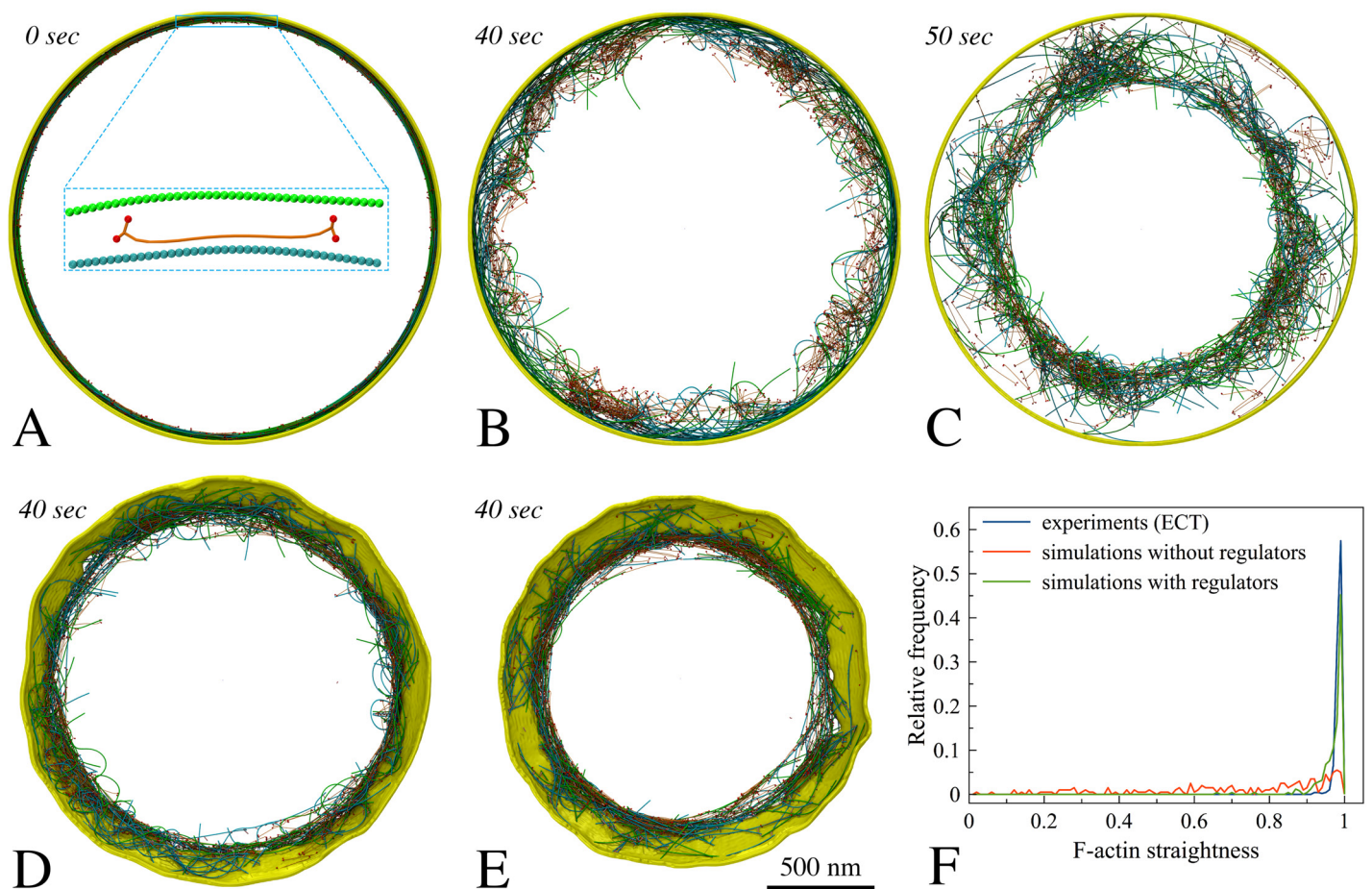
137  
138 **Figure 1:** Coarse-graining the actomyosin system: (A) Models of F-actin (green), myosins (tail in orange, heads in red), actin  
139 crosslinkers (pink), and membrane (yellow) (see text for details). Note the same visualizations and colors in the right are used for all  
140 following figures unless otherwise stated. (B) The ATPase cycle of myosin was modeled in five steps: myosin (1) binds ATP and  
141 releases actin, (2) hydrolyzes ATP, (3) binds actin, (4) releases phosphate, and (5) releases ADP.  
142

### 143 **F-actin straightness regulatory factors**

144 At this stage, the simulated F-actin did not mimic the consistently straight filaments observed experimentally  
145 (16), but they were highly bent (Fig. 2D, F, SI Appendix/Fig. S1). To study how the myosin processivity  
146 would influence bending, we reduced the myosin duty ratio (see [Methods/Myosin ATPase cycle](#) for the  
147 definition). As the first step of the ATPase cycle was slowed down 5 and 10 times, the duty ratio was reduced  
148 from the original value of  $\sim 0.72$  to 0.35 and 0.21, slowing down ring constriction and delaying filament

149 bending, but this did not eliminate bending. Inspecting the simulation results, we identified at least two factors  
150 that contributed to filament bending. First, if an F-actin was crosslinked close to its minus end while myosin  
151 was walking toward its free plus end, the plus end was pulled toward the minus end, bending the filament  
152 (Movie S1, at 3:42). As one proposed ability of F-actin is tension sensing (38), and myosin is known to bind  
153 preferentially to F-actin under tension (39), we added a rule that myosin could bind to actin only if the  
154 filament was crosslinked upstream. Note that even if we had tracked them in the simulation, other binding  
155 events would not have contributed tension since loose filaments simply move when pulled.

156



157

158 **Figure 2:** Setting up basic components of the simulated constriction system: F-actin (opposing polarities in green and cyan), bipolar  
159 myosin, crosslinkers, and membrane. Italic fonts indicate simulation times. (A) The initial ring was composed of F-actin, bipolar  
160 myosin and membrane. (B) The actomyosin ring did not contract in the absence of crosslinkers. (C) In the presence of crosslinkers,  
161 the ring did contract. (D) Adding tethers between F-actin and the membrane caused the ring to constrict the membrane. (E) Adding  
162 regulatory factors (tension-dependent interaction between actin and myosin, filament orientation-dependent crosslinking, cofilin

163 function, and actin turnover) reduced F-actin bending. (F) Histogram of straightness factors for filaments visualized by ECT (16)  
164 (blue), simulations without regulatory factors (red), and with regulatory factors (green).

165

166 Second, if an actin filament had each of its ends crosslinked to two different filaments sliding toward one  
167 another, the filament would bend (Movie S1, at 4:03). We reasoned that bending was not seen *in vivo* because  
168 either (i) crosslinks were released on the bent filament or (ii) the filament was broken. Hypothesizing that  
169 torque facilitates crosslink release, we added a rule that the probability of crosslink release increases with the  
170 angle between two filaments at their crosslinked location (Methods/Torque-facilitated crosslinker release  
171 for details). Next, considering that the actin-depolymerizing factor cofilin preferentially severs F-actin that is  
172 not under tension (40), we introduced its function into the simulation by stipulating that the probability of  
173 filament breaking increases with bending angle (Methods/Cofilin function for details).

174

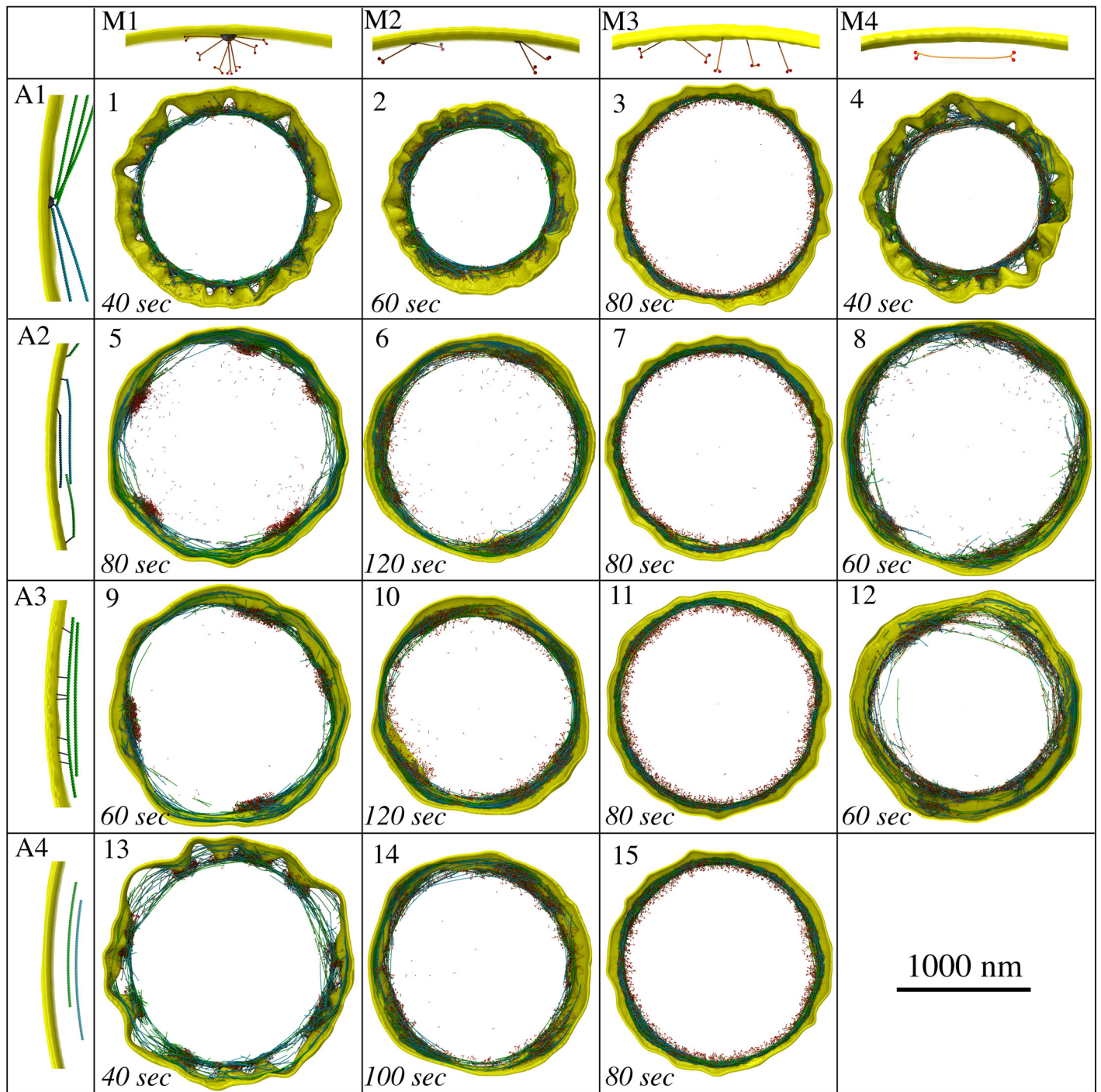
175 Another factor that might affect F-actin bending is actin depolymerization, which has been shown to occur  
176 rapidly during constriction (41). Actin turnover was therefore added (Methods/Protein turnover for details).  
177 Further, turnover of myosin and crosslinkers was also implemented (Methods/Protein turnover for details)  
178 since this occurs in fission yeast (29, 41, 42). In the presence of these regulatory rules, F-actin bending was  
179 prevented *in silico* (Movie S1, at 5:04; Fig. 2E, F), thus recapitulating the filament straightness observed  
180 experimentally (16).

181

## 182 **Exploration of actomyosin architecture models**

183 Having established a working core model, we explored fifteen plausible configurations and arrangements of F-  
184 actin and myosin to study how they would constrict the membrane (Fig. 3). We reasoned that the membrane  
185 must be tethered to either actin or myosin, or both, to enable membrane constriction. The four configurations  
186 of actin are illustrated in Fig. 3 (panels A1–A4). In (A1), F-actin plus ends were tethered to 64 membrane-  
187 bound nodes, as shown for ring assembly (20, 43). In (A2), the plus end of each F-actin was tethered to a  
188 random membrane bead. In (A3), tethering could occur on any actin bead along the filament, and in (A4) F-

189 actin was not tethered to the membrane. The four configurations of myosin are illustrated in [Fig. 3 \(panels](#)  
190 [M1–M4](#)). In (M1), unipolar myosins were tethered by their tails to 64 membrane-bound nodes, again, as  
191 shown for ring assembly ([20, 43](#)). In (M2), unipolar myosins were tethered to the membrane in pairs. In (M3),  
192 each unipolar myosin was tethered to a random membrane bead and in (M4), myosins were modeled as  
193 bipolar molecules, randomly distributed throughout the ring, unattached to the membrane. The basic principles  
194 of constriction that were discovered are presented below.  
195



196

197

198

199

200

201

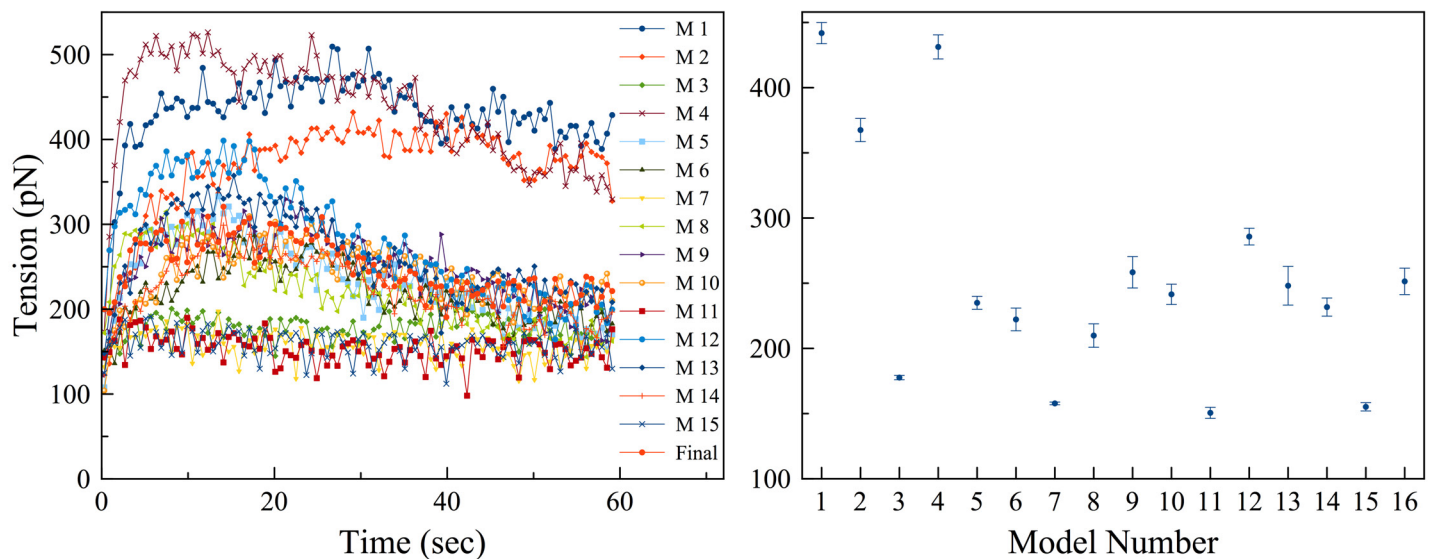
202

**Figure 3:** Exploration of different actomyosin models resulting from combining four actin configurations (A1–A4) with four myosin configurations (M1–M4). Resultant snapshots of the fifteen plausible models are presented. Note that the combination of A4 and M4 is not plausible since there are no tethers between the contractile ring and the membrane.

## 203 **Ring tension**

204 First we calculated the ring tension of all the models (Fig. 4). In models where actin and myosins were  
205 anchored to pull on one another in a tug-of-war fashion (e.g., model 1–4 where actin was connected in nodes,  
206 model 3 being an exception), the ring produced a large tension. Meanwhile the ring produced a small tension  
207 if myosins were unipolar and individually attached to the fluidic membrane (models 3, 7, 11, 15). All models,  
208 however, produced tensions of similar order to the ring tension observed experimentally (24). This suggests  
209 that, at least within our models, comparison of the ring tension is not a definitive criterion to rule out certain  
210 models.

211



212

213 **Figure 4:** The ring tension was calculated: (left) representative individual time courses of the ring tensions, and (right) their averages  
214 over 5 simulations produced by 16 models with number 16 representing the final model. Error bars represent standard deviations.

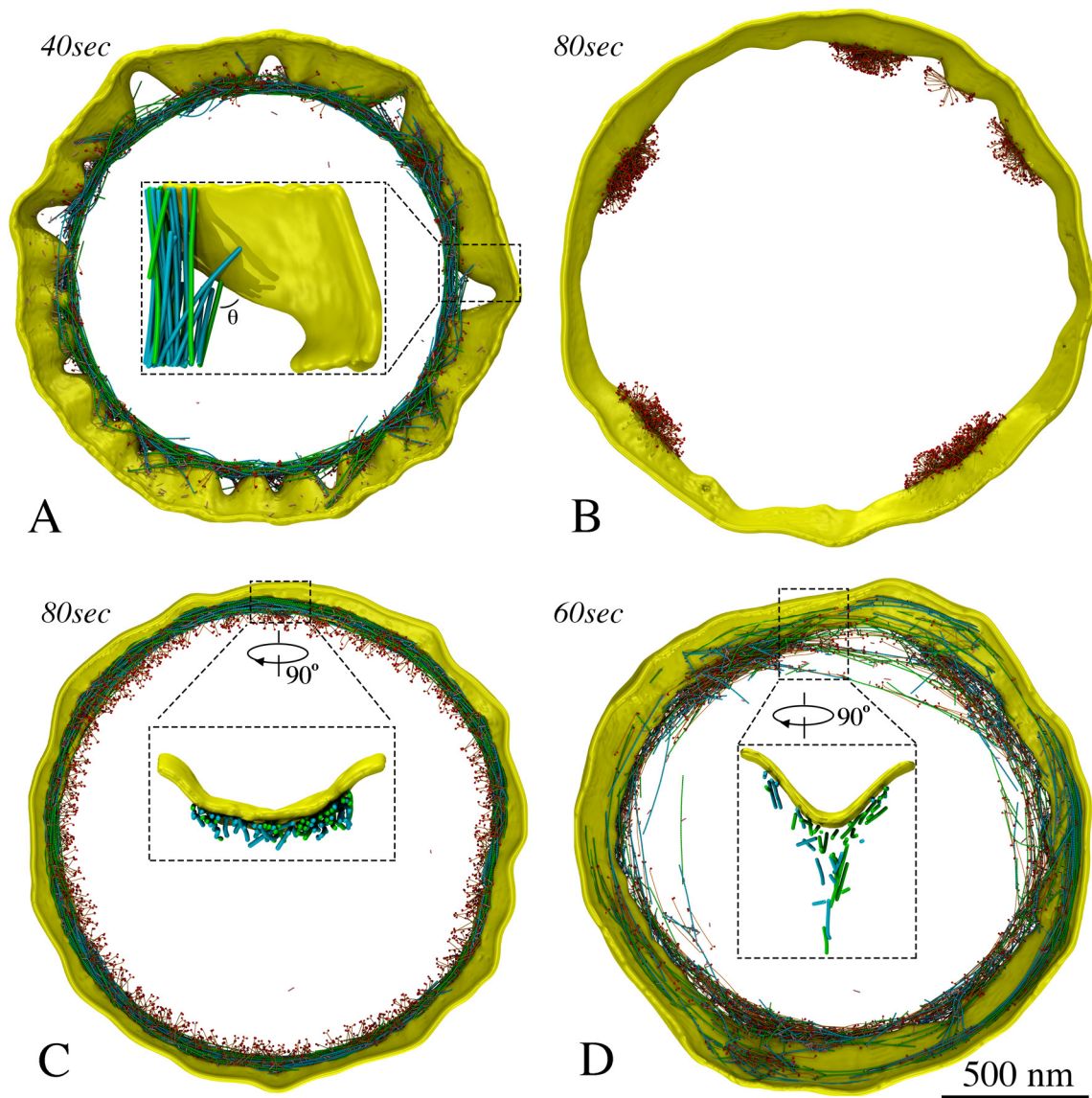
215

## 216 **Individually, homogeneously distributed unipolar myosins maintain membrane smoothness**

217 Several scenarios led to loss of membrane smoothness and circularity. One obvious cause was focusing the  
218 constriction force on only a small number of membrane sites. The most severe distortion occurred when the  
219 ring was connected to the membrane via only 64 nodes, as in models 1, 4, and 13, which resulted in membrane  
220 puckering during constriction (Fig. 3; SI Appendix/Fig. S2 & S3; Movie S1, at 7:08). As new cell wall  
221 material filled the gap between the membrane and the cell wall, puckering also occurred on the leading edge of

222 the septum (SI Appendix/Fig. S2B, right panel), supporting the membrane puckers against turgor pressure. We  
223 found that our fluidic membrane model allowed nodes to slide (Fig. S4) with speeds comparable to those  
224 during ring assembly reported experimentally and via simulations (15, 37). As a result of node sliding, in  
225 several cases, puckers coalesced making large membrane deformations (Fig. S2C; Movie S1, at 7:50). Neither  
226 reducing the concentrations of actin, myosin, and crosslinkers in half (SI Appendix/Fig. S2C) nor doubling  
227 them (SI Appendix/Fig. S2D) mitigated puckering. The defects persisted even as the number of nodes  
228 increased from 64 to 140 (SI Appendix/Fig. S2E); the latter was recently reported by Laplante et al (27). We  
229 then studied how puckering depended on the mechanosensitivity of cell wall growth by varying  $F_m$ , the  
230 minimal radial force on a membrane bead that induces cell wall growth (defined in **Methods/Cell wall and**  
231 **turgor pressure**). Increasing  $F_m$  100 times suppressed cell wall growth when unipolar myosins were  
232 individually connected to the membrane, but this low mechanosensitivity did not prevent nodes-induced  
233 puckering (SI Appendix/Fig. S5). Because the membrane in every cryotomogram appeared smooth (16), we  
234 know small puckers do not form in vivo, noting however that puckers larger than the 200 nm-thick  
235 cryosections cannot be ruled out. In our simulations, the presence of membrane puckers often caused actin  
236 filaments to lie at large angles with respect to the membrane (Fig. 5A; SI Appendix/Fig. S2B; S3B; S3C). By  
237 contrast, in other models which did not produce membrane puckers, filaments remained parallel to the  
238 membrane (Fig. 6), which is consistent with experimental observation (16). Smaller membrane puckers were  
239 observed in model 2, where unipolar myosins were attached to the membrane in pairs (Fig. 3; SI  
240 Appendix/Fig. S3A; Movie S1, at 8:11). On the other hand, in models 3, 7, 11 and 15, where unipolar myosin  
241 was individually attached to the membrane, providing an abundance of attachments, the membrane constricted  
242 without losing smoothness and actin filaments stayed parallel to the membrane (Fig. 3; Fig. 6; SI  
243 Appendix/Fig. S6; Movie S1, at 11:27). Therefore, if unipolar myosins exist during constriction, they are  
244 likely attached to the membrane individually.

245



246

247 **Figure 5:** Representative features produced by the fifteen models. (A) Membrane puckering, as occurred in model 1, and large  
248 angles between filaments and membrane. (B) Tethering membrane-bound unipolar myosins in nodes or pairs, as in columns 1 and 2  
249 of Fig. 3, resulted in aggregation. (C) Individual unipolar myosins, as in model 11, pulled filaments close to the membrane. (D)  
250 Bipolar myosins, as in model 12, pulled filaments away from the membrane.

251

252 Since a previous study observed that during ring assembly, actin and myosins in a broad band of nodes could  
253 coalesce into different structures when the crosslinker concentration varied (37), we explored whether  
254 changing the crosslinker concentration influenced the ring architecture in our simulations. Doubling or halving  
255 the crosslinker concentration did not change the ring architecture or basic outcome of any of our constriction  
256 models.

257

## 258 **Attaching unipolar myosin individually to the membrane prevents aggregation**

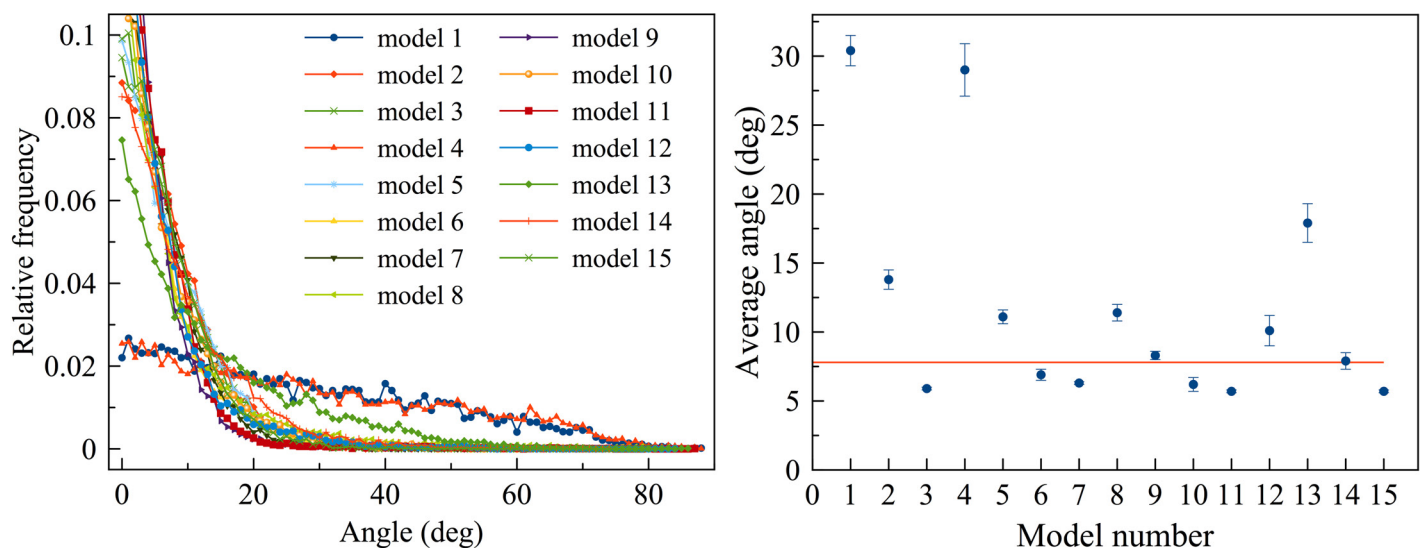
259 Among models with abundant membrane attachments, in 5, 6, 9, 10 and 14 membrane deformation still  
260 occurred due to myosin aggregation. In contrast to fluorescence microscopy observations (44, 45, 22),  
261 myosins in these models gradually clumped together into a few large aggregates along the ring (Fig. 5B).  
262 Aggregation of unipolar myosins occurred through entanglement as either membrane nodes (models 5 and 9;  
263 Fig. 3; SI Appendix/Fig. S7; Movie S1, at 8:31) or pairs of myosins (models 6, 10 and 14; Fig. 3; SI  
264 Appendix/Fig. S8; Movie S1, at 9:12) became caught on each other due to steric hindrance while sliding along  
265 the membrane. Entangled myosin clusters were in turn larger, increasing the chance for further entanglement  
266 and creating a positive feedback that exaggerated the defect as constriction proceeded. As aggregation  
267 eventually concentrated the constrictive force, membrane circularity was lost. Varying the myosin turnover  
268 rate in models 6, 10, and 14, we found that myosin aggregation was mitigated when the myosin turnover rate  
269 was increased to 15 times faster or more than the rate we observed experimentally (SI Appendix/Fig. S9;  
270 Table S1). In model 8, where actin plus-ends were tethered to the membrane and bipolar myosin was not,  
271 clustering of plus-end tethers also led to myosin aggregation at these locations (Fig. 3; SI Appendix/Fig. S10;  
272 Movie S1, at 10:23). In contrast, in models 3, 7, 11 and 15, the uniform distribution of myosin provided a  
273 persistent, homogenous distribution of constrictive force that preserved membrane smoothness and circularity  
274 (Fig. 3; SI Appendix/Fig. S6; Movie S1, at 11:27) further supporting the notion that unipolar myosins are  
275 individually tethered to the membrane.

276

## 277 **Bipolar myosins pull actin filaments away from the membrane**

278 Next, we focused on the five models where the membrane remained smooth (models 3, 7, 11, 12 & 15) and  
279 measured the distance between F-actin and the membrane (SI Appendix/Fig. S11). The four models containing  
280 individually tethered unipolar myosins (models 3, 7, 11 & 15) restricted filaments to ~21 nm from the  
281 membrane (Fig. 5C; SI Appendix/Fig. S6; Fig. S11), while ECT showed an average distance of ~60 nm (16).

282 Due to membrane-tethering and pulling forces from the unipolar myosins, less than 0.2% of the actin beads in  
283 these four models were at a distance larger than 60 nm. In model 12, untethered bipolar myosins tended to pull  
284 actin away from the membrane, producing a larger average distance of 32 nm with nearly 10% of the actin  
285 beads at a distance larger than 60 nm (Fig. 5D; SI Appendix/Fig. S11). This suggested the presence of bipolar  
286 myosin within the ring in real cells. In some cases, actomyosin bundles consisting of unattached F-actin and  
287 bipolar myosins peeled off from the ring and depolymerized (Fig. 5D; Movie S1, at 10:51). This is consistent  
288 with previous observations by fluorescence microscopy (22), further supporting the presence of bipolar  
289 myosins and suggesting that actin filaments are not attached to the membrane.  
290



291  
292 **Figure 6:** Angles between actin filaments and the membrane calculated after 60 sec of simulated time: (left) representative  
293 histograms of angles in individual simulations and (right) averages over five simulations for each model with error bars representing  
294 standard deviation and the red horizontal line indicating the average angle ( $7.8^\circ$ ) measured from electron tomograms for a reference.  
295 The presence of puckers, as in models 1, 4, and 13, causes filaments to form angles larger than observed experimentally.

296

### 297 **Final model: dual myosin configurations**

298 We therefore built a final model consisting of untethered F-actin, individual unipolar myosins, and bipolar  
299 myosins (Fig. 7A). Simulating the final model resulted in normal constriction without visible defects of the  
300 membrane or ring (Fig. 7B; Movie S1, at 13:27). In this model, unipolar myosins remained at the outer edge

301 of the ring due to their membrane attachment, while the bipolar form drifted inward, pulled toward the center  
302 by interaction with F-actin (Fig. 7C; Movie S2, at 13:54), matching the fluorescence microscopy result of the  
303 two myosin isoforms Myo2p and Myp2p (22). In our simulations, interactions with bipolar myosins pulled  
304 actin filaments away from the membrane (Fig. 7B, zoomed-in view; Fig. 7D), approximately recapitulating the  
305 distances observed by ECT (16), and occasionally caused actin/bipolar myosin bundles to peel off, as reported  
306 previously for actin/Myp2p bundles (22). Reducing the ATPase rate of the unipolar myosin in the simulation  
307 caused actin/bipolar myosin bundles to peel off more frequently, again in agreement with fluorescence  
308 microscopy results in which the loss of actin/Myp2p bundles occurred at higher frequency when the  
309 biochemical activity of Myo2p was reduced (22).

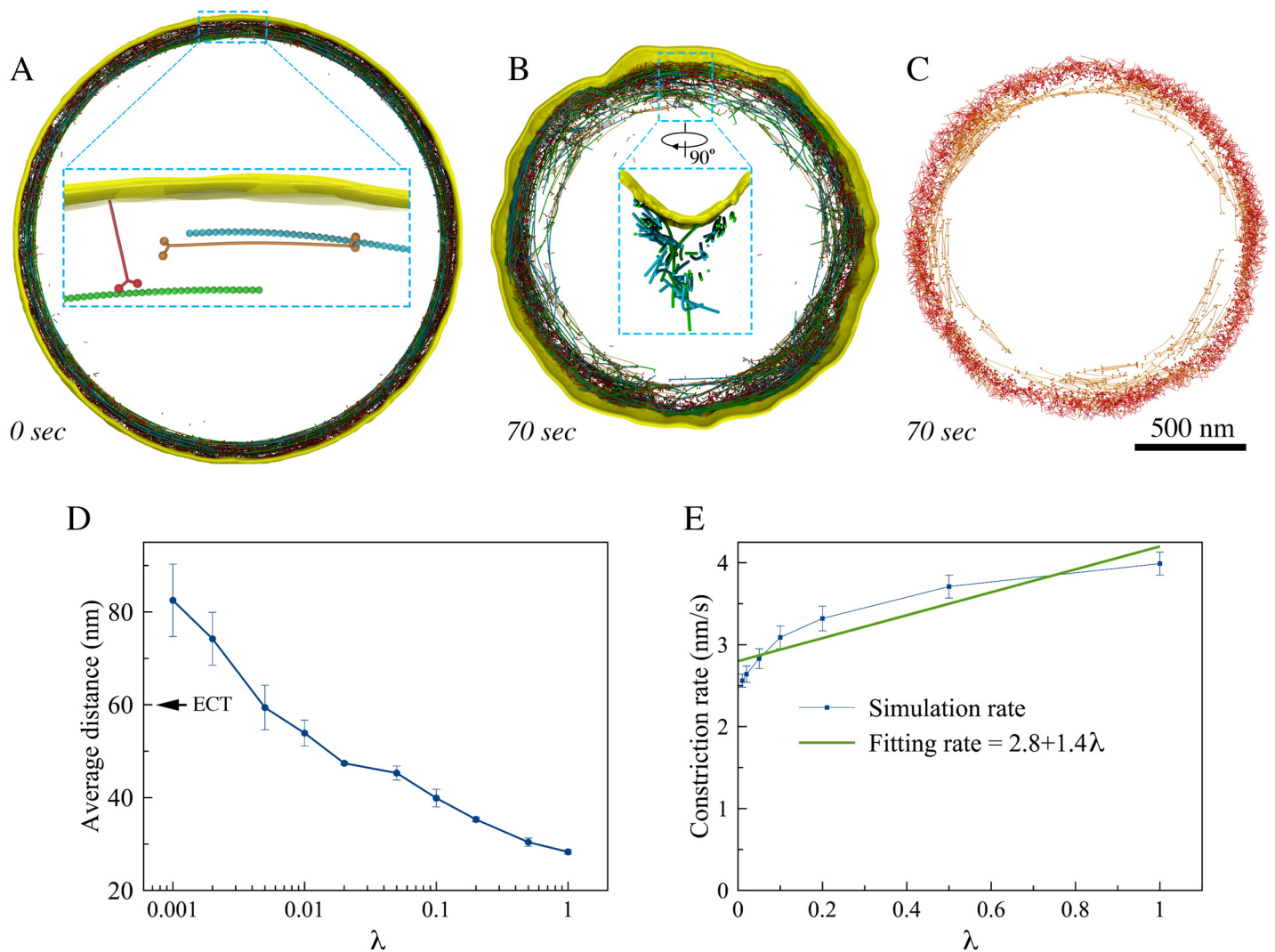
310

311 Reasoning that the balance of force between unipolar myosins pulling F-actin close to the membrane and  
312 bipolar myosins pulling it away would dictate its average distance to the membrane, we investigated how the  
313 average distance between F-actin and the membrane depended on the ATPase rate of the unipolar myosin by  
314 scaling it with a factor  $\lambda$ . As expected, the average distance between F-actin and the membrane increased as  
315 the ATPase rate of the unipolar myosin decreased, reaching the experimentally measured value of 60 nm at  
316  $\lambda \sim 0.005$  (Fig. 7D).

317

318 To further dissect the roles of the two forms of myosin, we studied the simulated constriction rate,  $v = \Delta r / \Delta t$ ,  
319 defined as the ratio of average inward radial growth of the cell wall  $\Delta r$  to constriction time  $\Delta t$ , as a function of  
320 the unipolar myosin's ATPase rate (scaled with factor  $\lambda$ ) (Fig. 7E). For simplicity,  $v$  was considered a linear  
321 combination of contributions from the bipolar myosin  $v_b$  and the unipolar myosin  $v_u$ . Fitting  $v = v_b + v_u \lambda$  to  
322 the simulated data yielded  $v_b = 2.8$  nm/s and  $v_u = 1.4$  nm/s. Since there were 2,000 bipolar and 3,200  
323 unipolar myosin heads, on average, each bipolar head contributed an amount of  $\sim 1.4$  pm/s to the constriction  
324 rate while each unipolar head contributed  $\sim 0.4$  pm/s. The efficiency of the bipolar myosins in our simulations  
325 was therefore several times that of the unipolar myosins, likely due to the fact that unipolar myosins were

326 attached to the fluidic membrane. This is in agreement with the experiments that showed Myp2p contributes  
 327 more to the constriction rate of real cells than Myo2p (22).  
 328



329  
 330 **Figure 7:** The final model. (A) A zoomed-in view shows initial configuration of the ring, including untethered F-actin (green and  
 331 cyan), membrane-attached unipolar myosins (red), and bipolar myosins (orange). During constriction, (B) membrane smoothness  
 332 and circularity were preserved and distances between F-actin and the membrane as observed in tomograms were recapitulated (as  
 333 shown in a zoomed-in view), and (C) the membrane-attached unipolar myosins (red) occupied the outer edge of the ring while the  
 334 unattached bipolar myosins (orange) occupied the inner edge. (D) Average distance between the simulated F-actin and the  
 335 membrane (arrow indicates the average distance measured in tomograms) and (E) constriction rate as a function of the unipolar  
 336 myosin's ATPase rate scaling factor,  $\lambda$ . Error bars represent standard deviations ( $n = 5$ ).

## 337 **Discussion**

338

339 From a methodological standpoint, we have demonstrated how 3D coarse-grained simulations can be used to  
340 explore complex models and hypotheses. The ring components were modeled in individual molecular detail,  
341 exerting force on a flexible membrane. Individual steps of myosin II's ATPase cycle were also modeled to  
342 produce power-stroke-driven movement of myosin along actin filaments. While we could not of course  
343 include all relevant molecules (only ~4 of the more than 100 proteins involved were modeled) or fully explore  
344 parameter space, our results did nevertheless suggest several interesting principles.

345

### 346 **The role of crosslinkers**

347 Previous experimental studies have shown that crosslinkers such as  $\alpha$ -actinin and fimbrin are essential for  
348 assembly of the fission yeast's AMR ring, but their role during constriction has not been clear (28–30). Earlier  
349 simulations showed that end-tracking crosslinkers and actin filament depolymerization could together drive  
350 contraction (36), but  $\alpha$ -actinin and fimbrin are not end-tracking, and it remains unclear whether end-tracking  
351 crosslinkers are present in the ring. It was also previously suggested that contractility could arise in the  
352 presence of thick myosin filaments if they functioned as crosslinkers by remaining bound to the barbed end of  
353 F-actin (46). Although this might promote connectivity for long-range propagation of tension, it was unclear  
354 how such binding would be maintained, and thick myosin filaments were not seen in the cryotomograms (16).  
355 Our simulations suggest that crosslinkers like  $\alpha$ -actinin and fimbrin allow long-range propagation of tension  
356 around the ring. This is consistent with findings on the contractility of *in vitro* ring-like (47) and disordered  
357 networks of actin (48).

358

### 359 **F-actin straightness**

360 ECT revealed that F-actin filaments in dividing cells are remarkably straight (16). While in our first  
361 simulations involving only F-actin and myosin, the actin filaments became highly bent, here we identified two

362 factors that likely reduce this bending *in vivo*. First, it has been shown *in vitro* that myosin binds preferentially  
363 to F-actins under tension (39). Biasing myosins to preferentially bind stretched F-actin filaments in our  
364 simulations reduced bending, and also helped maintain ring tension. It has also been shown *in vitro* that cofilin  
365 preferentially severs F-actins not under tension (40). Biasing cofilin's activity to bent filaments here promoted  
366 filament straightness. Our simulations therefore suggest one rationale for the otherwise puzzling presence in  
367 the ring of an actin severing factor (32, 33).

368

### 369 **Comparisons to previous simulations/treatments of actomyosin systems**

370 Dasanayake et al. (49) studied 2D disordered networks of actin, myosin, and crosslinkers and found that they  
371 were by nature contractile, in agreement with our findings for the interplay of these three basic elements.  
372 Lenz also explored the behavior of disordered 2D networks, and found analytically that “contractile forces  
373 result mostly from motors plucking the filaments transversely” (50). The architecture of the AMR is very  
374 different, since the actins are parallel and bundled into a ring. As a result, contractile forces in our simulations  
375 arose from motors sliding parallel filaments past each other. Stachowiak et al. simulated a 2D actomyosin  
376 band where nodes containing 40 bipolar myosins each were modeled as single beads (24). The authors  
377 observed clustering of myosin beads when protein turnover was stopped, but the cause of aggregation was  
378 very different than seen here because in their model volume exclusion was not applied to all elements (e.g.,  
379 objects could pass through actin filaments). In contrast, by modeling all the basic elements (including the  
380 membrane) in 3D and applying volume exclusion to all objects, we found aggregation occurred when actin  
381 filaments and unipolar myosins were connected to the membrane in nodes or pairs, throughout a range of  
382 physiologically relevant turnover rates. Further, our simulations allowed the characteristics and consequences  
383 of different actomyosin configurations to be assessed in 3D, and compared directly with those observed in  
384 cryotomograms (16). This revealed that concentrating force at nodes produces puckers in the membrane.  
385 Moreover, while Stachowiak et al.’s simulations produced tension similar to that measured in fission yeast  
386 protoplasts, our results showed that other actomyosin configurations can also produce ring tension of similar

387 order. The most closely related previous work was that of Bidone et al., (37), who simulated how actin nodes  
388 placed on a 3D cylindrical surface can be drawn together into a tight ring by myosin filaments. The major  
389 difference with our work is that while Bidone et al. explored assembly of the ring, ours explored contraction,  
390 including changes in the shape of the cell wall boundary, and we found that concentrating force at nodes  
391 results in puckers. Thiyagarajan et al. simulated septum closure with a 2D representation of the cell wall (45).  
392 Assuming that the ring follows the shape of the septum leading edge, a condition we interpret as requiring an  
393 intimate and uniform connection to the membrane, and that the rate of cell wall growth was proportional to  
394 radial force, Thiyagarajan et al. showed that cell wall growth in local depressions would be faster than in  
395 flatter regions, and this could maintain circularity. This is most like our model in which myosins were  
396 connected to the membrane individually, since then force was distributed across thousands of connections, and  
397 in our case, this architecture also maintained circularity. Our simulation went on to show, however, that when  
398 force was concentrated at nodes, the basic assumption of uniform connection broke down and puckers  
399 resulted.

400

#### 401 **Do nodes exist during constriction?**

402 Actin filaments and myosins have been shown to form nodes during the assembly of the ring (11–15, 51), but  
403 a more recent study reported that the head domain of Myo2p distributed along pre-constriction rings (52),  
404 reflecting a discrepancy in the literature. While Laplante et al. recently suggested nodes persist during  
405 constriction (27), our results call into question whether this is the case. In our simulations, whenever  
406 constrictive force was concentrated on nodes or aggregates, membrane puckers formed, which is intuitively  
407 reasonable and we are not surprised this is invariant across crosslinker concentrations, myosin processivity,  
408 turnover rates, etc. As a consequence, large angles were frequently created between F-actin and the membrane  
409 (Fig. 5A, SI Appendix/Fig. S2B; S3B; S3C), features not seen in the cryotomograms (16). We conclude that  
410 either nodes are not present during constriction or we don't understand yet what other cellular forces maintain

411 smooth membranes when constrictive force is concentrated at nodes. Perhaps future experiments will provide  
412 new insight into how membrane puckers are prevented.

413

#### 414 **Actomyosin architecture**

415 Instead of being directly attached to the membrane in nodes, our simulations suggest that actin filaments are  
416 not attached to the membrane. This rationalizes how bundles of actomyosin were able to separate from the  
417 membrane in fluorescence microscopy experiments (22). Our simulations also favored models where unipolar  
418 myosins link the ring and the membrane. While no clear evidence of such connections were seen in  
419 cryotomograms (16), the coiled-coil tail of a unipolar myosin is too thin and flexible to be resolved by ECT.  
420 Considering that Myo2p is the only myosin essential for viability (6, 21), it is a reasonable candidate for this  
421 role. Unipolar Myo2p molecules have already been proposed to attach to the membrane at nodes during ring  
422 assembly (20), but our results suggest they are more likely attached to the membrane individually to prevent  
423 aggregation and preserve membrane smoothness and circularity. Further, our results suggest that the myosin  
424 isoform Myp2p may exist in a bipolar configuration within the ring. This would explain fluorescence light  
425 microscopy experiments that showed that Myp2p primarily drives constriction, occupies the inner subdomain  
426 of the ring, and causes actomyosin bundles to peel away from the ring (22).

427

## 428 **Methods**

429 For convenience, the key parameters of our simulations are listed in [SI Appendix/Table S2](#).

430

### 431 **Actin filament**

432 We modeled the actin filament (F-actin) as a chain of beads connected by springs ([Fig. 1](#)). Considering the  
433 double-helical nature of the filament, for convenience, each model bead represented two globular actin  
434 monomers (G-actin). Since 13 G-actins, corresponding to 6.5 model beads, cover a length of 35.9 nm ([53](#)), the  
435 relaxed length of the connecting spring is  $l_a = 5.5$  nm. The tensile modulus of F-actin has been measured to  
436 be  $E = 1.8$  nN/nm<sup>2</sup> ([54](#)). Estimating the cross-section of F-actin to be  $A \sim 30$  nm<sup>2</sup> we derived the force  
437 constant of our model springs to be  $k_a = EA/l_a \sim 10$  nN/nm, reflecting that F-actin is not easily stretched. To  
438 reduce the computational cost of simulating such stiff springs, however, we used a force constant of 1 nN/nm  
439 considering the fact that the stretching of the F-actin was still negligible with this constant. To recapitulate  
440 actin's semi-flexibility, bending at a bead with an angle  $\theta$  was penalized with an energy of  $E_\theta^a = k_\theta^a(\theta -$   
441  $\theta_0)^2/2$  where  $\theta_0 = 180^\circ$  was the relaxed angle, and the bending stiffness constant  $k_\theta^a$  was derived using the  
442 measured persistence length,  $L_p \sim 10$   $\mu$ m ([55](#)), to be  $k_\theta^a = k_B T L_p / l_a = 7.4 \cdot 10^{-18}$  J where  $k_B$  is the  
443 Boltzmann constant, and  $T = 295$  K is the room temperature. Note that in initial simulations (see [F-actin](#)  
444 [straightness regulatory factors](#)) filaments became highly bent with the original bending stiffness  $k_\theta^a = 7.4 \cdot$   
445  $10^{-18}$  J, but bending was prevented in the presence of straightness regulatory factors ([SI Appendix/Fig. S1](#)).  
446 Bending was also prevented even after  $k_\theta^a$  was reduced three times to  $2.4 \cdot 10^{-18}$  J, confirming that this  
447 reduction did not change the outcome of our simulations. Again, to reduce the computational cost, we then  
448 used  $k_\theta^a = 2.4 \cdot 10^{-18}$  J for the rest of our simulations.

449

### 450 **Myosin configuration**

451 Myosin was modeled to be either unipolar or bipolar and the same parameters were used for both  
452 configurations. Unipolar myosin was modeled as an 8-bead tail (representing the elongated C-terminal coiled-

453 coil tail domain of two myosin heavy chains) connected to two head beads representing the N-terminal motor  
454 domains of the two heavy chains (Fig. 1). Bipolar myosin was composed of two unipolar molecules connected  
455 at the tails. Like the actin filament, the beads were connected by springs of force constant  $k_m = 1$  nN/nm, and  
456 relaxed length  $l_m = 10$  nm, which was chosen to reproduce a length of  $\sim 80$  nm reported for the fission yeast  
457 conventional myosin II (56). To recapitulate the experimentally reported pulling force of 3–4 pN by a single  
458 myosin head (57), simulations were done where a unipolar myosin interacted with an actin filament from  
459 which the bending stiffness constant was determined to be  $k_\theta^m = 0.5 \cdot 10^{-18}$  J (SI Appendix/Fig. S12). The  
460 relaxed angle was  $180^\circ$  on the tail, but at the head-to-tail junction it varied depending on the ATPase status of  
461 the head bead (see below for details).

462

### 463 **Myosin ATPase cycle**

464 To model interaction with actin, each myosin head was allowed to exist in five phases: bound to (i) ATP, (ii)  
465 ADP and the hydrolyzed  $P_i$ , (iii) ADP,  $P_i$  and actin, (iv) ADP and actin ( $P_i$  was released), and (v) actin (ADP  
466 was released). The relaxed angle at the head-tail junction was  $120^\circ$  if the myosin head was in phases (ii) or  
467 (iii) and  $60^\circ$  if in phases (i), (iv), or (v). Since ATPase rates for the individual phases of myosin II in fission  
468 yeast are not known, the probabilities of each phase transition were calculated based on studies from different  
469 species (58, 59). Specifically, ATP hydrolysis (phase (i) to (ii) transition) occurred with a probability of  $p_1 =$   
470  $25/s$ . If a myosin head in phase (ii) was within an interaction distance  $D = 15$  nm from an unbound actin bead,  
471 actomyosin binding (phase (ii) to (iii) transition) occurred with a probability of  $p_2 = 50/s$ . If there were more  
472 than one actin bead within  $D$ , the probability of being chosen for actin bead  $i$  was calculated as

$$473 \quad P_i = f_i / \sum f_i \quad [1]$$

474 where  $f_i = d_0^2(D^2 - d^2)/[d^2(D^2 - d_0^2)]$  was a function of the distance  $d$  between the myosin head and  
475 actin bead  $i$  and  $d_0 = 5$  nm was the relaxed distance between them once they were bound to each other.

476 Myosin II is known to walk on F-actin directionally from the pointed end to the barbed end. To model this  
477 property, for simplicity, binding between myosin and actin was allowed only if the angle  $\theta$  formed by the

478 head-to-tail myosin vector and the plus-to-minus end actin vector was smaller than  $90^\circ$  (SI Appendix/Fig.  
479 S13A). Release of  $P_i$  (phase (iii) to (iv) transition) occurred with a probability of  $p_3 = 25/s$ , generating a  
480 pulling force in a power stroke fashion as the head-tail angle relaxed from  $120^\circ$  to  $60^\circ$ . ADP release (phase  
481 (iv) to (v) transition) occurred with a probability of  $p_4 = 25/s$ . Finally ATP binding and actin release (phase  
482 (v) to (i) transition) occurred with a probability of  $p_5 = 150/s$ . Our implemented rates of the myosin ATPase  
483 cycle resulted in an average myosin duty ratio of  $(\sum_{i=2}^5 1/p_i)/(\sum_{i=1}^5 1/p_i) = 0.72$ . While these rates set the  
484 upper limit of the load-free velocity of a myosin molecule to  $l_m/(\sum_{i=1}^5 1/p_i) = 70$  nm/s, a previous  
485 experimental study reported a myosin load-free velocity of 500 nm/s (60), reflecting a discrepancy in the  
486 literature.

487

## 488 Actin Crosslinkers

489 Crosslinkers were modeled as two actin-binding domain (ABD) beads connected to a central bead by two  
490 springs of a force constant  $k_c$  and relaxed length  $l_c$  (Fig. 1). To account for the existence of different potential  
491 crosslinkers in real cells, namely  $\alpha$ -actinin and fimbrin (30), two types of crosslinkers were modeled. The one  
492 representing  $\alpha$ -actinin had a length of  $2l_c^\alpha = 22$  nm, the combined length of two ABDs (5 nm each) and two  
493 spectrin repeats (6 nm each) estimated from PDB structure 4D1E (while human  $\alpha$ -actinin has four,  $\alpha$ -actinin  
494 of fission yeast has only two spectrin repeats (61)), and  $k_c^\alpha = 0.5$  nN/nm. The other representing fimbrin had  
495  $2l_c^f = 10$  nm (estimated from PDB structure 1RT8) and  $k_c^f = 1.1$  nN/nm, which was chosen so that the two  
496 crosslinkers had the same Young's modulus, meaning  $k_c^\alpha l_c^\alpha = k_c^f l_c^f$ . To promote stiffness, bending with an  
497 angle  $\theta$  was penalized with an energy of  $E_\theta^{cl} = k_\theta^{cl}(\theta - \theta_0)^2/2$ , where  $\theta_0 = 180^\circ$  was the relaxed angle and  
498 the bending stiffness constant was  $k_\theta^{cl} = 0.5 \cdot 10^{-18}$  J. Note that the spring constant for crosslinkers in our  
499 model was four orders of magnitude larger than that used in a previous simulation work by Stachowiak et al.  
500 (24) where the authors sourced an experimental work by Claessens et al. (62). In our opinion, Stachowiak et  
501 al. misinterpreted  $k_{||} = 0.025$  pN/nm (which was defined by Claessens et al. as the crosslinker's effective

502 shear stiffness at very small deformations) as the crosslinker's extensional stiffness. Thermal forces would  
503 unrealistically stretch crosslinkers of this small spring constant tens of nm.

504

505 The binding of crosslinkers to actin was modeled to be stochastic. The binding of a crosslinker ABD bead to  
506 an actin bead within the interaction distance  $D = 15$  nm occurred with a probability of 100/s. Similar to  
507 myosin-actin binding, if there were more than one actin bead within  $D$ , the probability of being chosen for  
508 actin bead  $i$  was calculated using equation [1]. Actin release from  $\alpha$ -actinin and fimbrin occurred with  
509 probabilities of 3/s (63, 64) and 0.05/s respectively (28).

510

## 511 Membrane

512 The membrane was modeled as a single layer of beads initially forming a cylinder (Fig. 1). To preserve  
513 membrane integrity, attractive forces were introduced between neighboring beads. To do this, a mesh of non-  
514 overlapping triangles with vertices on the beads was calculated from which non-redundant pairs of neighbor  
515 beads were determined. If a pair of beads were separated at a distance  $d$  larger than  $d_{pair} = 20$  nm, they were  
516 pulled together with a force of  $F_{pull} = k_{pair}(d - d_{pair})^2$  where  $k_{pair} = 20$  pN/nm<sup>2</sup> was a force constant. To  
517 prevent the beads from being too close to each other, they were pushed apart with a force of  $F_{push} =$   
518  $k_{pair}(d_{mb} - d)^2$  if  $d$  was smaller than a distance  $d_{mb} = 10$  nm. Since a permanent pairwise interaction  
519 would have prevented membrane beads from moving away from one another, blocking fluidity, the non-  
520 overlapping triangle mesh and therefore the non-redundant pair list were recalculated every  $10^4$  steps. This  
521 allowed new pairs of beads to form based on their updated positions and made the membrane fluidic.

522

523 To generate membrane bending stiffness, a mesh of tetragons with vertices on the beads was calculated. If the  
524 four beads on each tetragon were not on the same plane such that the two diagonals were separated by a  
525 distance  $d$ , a spring-like force,  $F_{mb} = k_{mb}d$ , was exerted on the beads to pull the two diagonals towards each  
526 other (SI Appendix/Fig. S13B). Based on the reported membrane bending stiffness (65), the force constant

527 was calculated to be  $k_{mb} = 2$  pN/nm. To prevent boundary artifacts, we applied a periodic boundary condition  
528 by translating the images of the beads of one edge to the other.

529

### 530 **Torque-facilitated crosslinker release**

531 If two filaments were crosslinked at an angle  $\alpha$  that was larger than  $60^\circ$  (SI Appendix/Fig. S13C) then once  
532 every  $10^4$  time steps the crosslink was released with a probability  $P_{ux} = 0.5 - \cos(\alpha)$ .

533

### 534 **Cofilin function**

535 If at an actin bead, the angle  $\alpha$  between the tangent and the position vector from the barbed end (SI  
536 Appendix/Fig. S13D) was larger than  $60^\circ$ , once every  $10^5$  time steps (the number was arbitrarily chosen since  
537 the rate in real cells is not known) the filament was broken into two segments with a probability  $P_{br} = 1.0 -$   
538  $\cos(\alpha)$ .

539

### 540 **Protein turnover**

541 To model the turnover of ring components, actin depolymerization, addition of new F-actin, myosin removal  
542 and addition, and crosslinker removal and addition were included. At the beginning the G-actin pool was set  
543 empty for simplicity. Actin depolymerization was modeled to be stochastic, which removed an actin bead at  
544 the minus end to the G-actin pool with a probability of once every second, considering that F-actin turnover  
545 was reported to occur in about 1 min (41). A new filament of a randomly-selected length was added to a  
546 random location along the ring with a probability of once every  $10^5$  time steps if the G-actin pool had more  
547 than 100 monomers. If membrane-bound nodes were present, the barbed end of the added F-actin was tethered  
548 to a random node.

549

550 A simple turnover mechanism was modeled for myosin. If all the heads of a myosin molecule were unbound,  
551 it was removed and a new one was added to a random location along the ring with a rate  $r_t = 1/\tau$ , where  $\tau$

552 was the resident time of unbound myosins. For each model, we varied  $\tau$  and measured the resultant average  
553 resident time of all myosins (bound and unbound). We report the resultant average resident times (SI  
554 [Appendix/Table S1](#)) that were close to 14 s, our experimentally-measured resident time (SI [Appendix/Fig.](#)  
555 [S9](#)), which is half of the previously reported value (41, 42). To explore the role of myosin turnover, multiple  
556 simulations of each model were run with different values of  $\tau$ . The particular values used to produce each  
557 figure shown are listed in Table S1.

558

559 Similarly, to model crosslinker turnover, if both the ABD beads of a crosslinker were unbound, it was  
560 removed and a new one was added to a random location along the ring with a probability of once every 20 s  
561 (29).

562

### 563 **Protein binding force**

564 If an actin bead and its binding partner (either a myosin head or a crosslinker ABD bead) were “bound” to  
565 each other at a given time step (see rules above for when they were considered bound), they exerted force on  
566 one another through a spring-like force  $F_b = k_b(d - d_0)$ , where  $k_b = 0.1$  nN/nm was the force constant and  
567  $d_0 = 5$  nm was the relaxed distance.

568

### 569 **Volume exclusion**

570 To prevent the beads from overlapping with one another, if the distance  $d$  between any two beads was smaller  
571 than  $r_{off} = 5$  nm, they were pushed apart with a force  $F_V = k_V(r_{off} - d)^2 / (d - r_{on})^2$  to prevent them from  
572 approaching each other closer than  $r_{on} = 4$  nm, where  $k_V = 0.1$  nN.

573

### 574 **Membrane tethering**

575 How tethering the ring to the membrane was modeled depended on the actomyosin configuration. In the node  
576 models, in which either F-actin plus ends or unipolar myosin tails (or both) were tethered to the membrane-

577 bound nodes, each node was modeled as a bead connected to 10 nearest-neighbor membrane beads determined  
578 at the beginning. If the distance  $d$  between a node and a tethering counterpart, either an actin plus end, a  
579 unipolar myosin tail end, or a neighboring membrane bead, was larger than  $d_n = 20$  nm, the pair were pulled  
580 closer to each other with a force  $F_n = k_n(d - d_n)$ , where  $k_n = 0.2$  nN/nm was the force constant. In the  
581 paired-unipolar myosin configuration, for simplicity the two tail-end beads were tethered to a small node  
582 including 4 additional nearest-neighbor membrane beads. In the other models, direct tethering between one  
583 membrane bead to actin and/or unipolar myosin was modeled. If the distance  $d$  between an actin bead and its  
584 membrane tethering counterpart was larger than  $d_t = 30$  nm, the beads were pulled closer to each other with a  
585 force  $F_t = k_t(d - d_t)$ , where  $k_t = 0.18$  nN/nm was the force constant. If the distance  $d$  between a unipolar  
586 myosin tail-end bead and its membrane tethering counterpart was larger than  $d_{my} = 5$  nm, the beads were  
587 pulled closer to each other with a force  $F_{my} = k_{my}(d - d_{my})$ , where  $k_{my} = 0.2$  nN/nm was the force  
588 constant.

589

### 590 **Cell wall and turgor pressure**

591 Cell wall growth is needed to support ingression of the membrane since the tension from the AMR is not  
592 sufficient to counter the effect of large turgor pressure (66). Experiments have shown, however, that septum  
593 assembly slows down four folds (44, 66) and becomes misshapen in the absence of the contractile ring (16),  
594 suggesting ring constriction guides septum assembly in the normal condition. For simplicity, the membrane  
595 was treated as squeezable and the wall was modeled as a semi-rigid layer that expanded inwards following the  
596 membrane (SI Appendix/Fig. S14). The net force from turgor pressure and the cell wall on the membrane was  
597 modeled to follow Hook's law: a membrane bead at a distance  $d$  from the wall surface was pushed by a force  
598  $F_w = -k_w(d - d_0)$ , where  $k_w = 0.05$  pN/nm was the force constant and  $d_0 = 20$  nm was the relaxed  
599 distance between the membrane and the wall. Previously, Thiyagarajan et al. proposed a tension-sensitive cell  
600 wall growth model in which the cell wall grows in proportion to the radial force exerted by the ring on the  
601 membrane (45). Similarly, to model cell wall growth, once every  $10^3$  time steps, if the difference between  $d$

602 and  $d_0$  was more than 0.1 nm (corresponding to a radial force of  $F_m = 0.005$  pN), the wall moved inward  
603 0.01 nm.

604

605 Note that because it is not presently known what force would be required to initiate cell wall growth, this  
606 minimal radial force required to initiate cell wall synthesis (0.005 pN) was simply chosen as a value 20x  
607 smaller than the typical force from the ring ( $\sim 0.1$  pN). To explore the role of this mechanosensitivity  
608 parameter, simulations were also run with much larger  $F_m$  values. We found that at  $F_m = 0.5$  pN (increased  
609 100 times), there was essentially no cell wall growth in the model where unipolar myosins were individually  
610 connected to the membrane (distributing the ring constriction force homogeneously), but in the model where  
611 nodes were present, cell wall growth did occur, but puckers still formed (Fig. S5). Therefore, puckers were  
612 consistently the result of force concentration at nodes, not an artifact of a high mechanosensitivity.

613

## 614 **Diffusion**

615 To model thermal motion of the system we introduced random forces on the beads. Each Cartesian component  
616 was generated following a Gaussian distribution using the Box-Muller transformation (67). Each  
617 transformation converted two random numbers from a uniform 0 – 1 distribution,  $u_1$  and  $u_2$ , into two random  
618 numbers of a Gaussian distribution:

$$r_1 = \cos(2\pi u_2) \sqrt{-2 \ln(u_1)}$$

$$r_2 = \sin(2\pi u_2) \sqrt{-2 \ln(u_1)}$$

619 For a system of  $N$  particles,  $3N/2$  transformations were used to generate  $3N$  numbers. While a pseudo random  
620 force can be generated by integrating a Gaussian random distribution with the time step, to reduce the  
621 computational cost, the random force was simply obtained by scaling the Gaussian random number with a  
622 force constant  $k_r$ . To determine  $k_r$  for actin we ran simulations of free individual actin filaments in the  
623 presence of the random force and compared the simulated tangent correlation,  $\langle \cos\theta \rangle$ , over distance  $L$  to the  
624 theoretical value  $e^{-L/L_p}$  where  $L_p$  was the persistence length of the filament (SI Appendix/Fig. S15). We

625 found that the simulated tangent correlation matched the theory best at  $k_r = 20$  pN. We then used the same  
626  $k_r = 20$  pN for the random force on myosins and crosslinkers considering they were also cytoplasmic  
627 proteins. In the absence of relevant experimental measurements, we arbitrarily chose  $k_r = 5$  pN for the  
628 random force on the membrane.

629

### 630 **Initial ring configuration**

631 To determine a minimal list of basic components of the ring, our model started with an actomyosin ring 200  
632 nm wide (dimension along the long axis of the cell) and 30 nm thick (dimension along the radial direction)  
633 inside a membrane 300 nm wide and 1,000 nm in radius. The ring was composed of 400 F-actins of length  
634 chosen randomly in the range of 270 – 810 nm long (50 – 150 beads) resulting in ~30 – 40 filaments per ring  
635 cross-section, well within the range of 14 – 60 filaments observed by ECT (16). 800 bipolar myosins were  
636 included. To study the role of crosslinkers, 600  $\alpha$ -actinins and 1,000 fimbrins were added to the ring. Note  
637 that these protein concentrations were within the ranges reported experimentally (68).

638

639 The same parameters for the membrane and crosslinkers were used for all 15 actomyosin configurations. The  
640 ring started 200 nm wide and 60 nm thick. Note that bundles of actomyosin peeled off the ring during  
641 constriction in model 12, where actin filaments were directly tethered to the membrane (see **Membrane**  
642 **tethering**) and myosin was bipolar, and this was also observed in the ring that started 30 nm thick. Either 800  
643 bipolar (model 4, 8, 12) or 1,600 unipolar myosins (the other models) were present. The same ring  
644 configuration was used in simulations of the final working model except there were 1,600 unipolar and 500  
645 bipolar myosins coexisting in the system. In all modeled rings, F-actin existed in two opposing polarities.

646

### 647 **Ring boundary**

648 ECT showed that F-actins were strictly localized to the leading edge of the septum (16). This might be the  
649 result of either the ring tension or some physical barrier that was not distinguishable in the tomograms or both.

650 The septin cytoskeletal proteins were thought to serve as such a barrier as they form a pair of rings flanking  
651 the actomyosin ring during constriction (69). This proposal was challenged later as the septin rings were  
652 reported to be dispensable for cytokinesis in budding yeast (70). In addition, the barrier function of septins is  
653 unlikely in fission yeast since the two rings do not contract during contraction of the actomyosin ring (12, 71,  
654 72). Another barrier candidate, if required at all, could be the F-BAR protein Cdc15, as it was reported to form  
655 long filaments likely wrapping around the division site several times (73). This stable scaffold might restrict  
656 movement of partner proteins in the ring. To implement a diffusion barrier in our model, if a ring component  
657 bead moved a distance  $\Delta x$  outside the ring boundary, chosen to be 200 nm wide along the ring axis, it was  
658 simply pulled back with a force of  $k_{br}\Delta x$ , where  $k_{br} = 10$  pN/nm was the force constant.

659

## 660 System dynamics

661 To track the evolution of the system we used a simple molecular dynamics simulation. Specifically, the  
662 coordinate  $X(t)$  of each bead changed following the Langevin equation:

$$M \frac{d^2 X}{dt^2} = -\nabla U(X) - \gamma \frac{dX}{dt} + R(t)$$

663 where  $M$  is the mass of the bead,  $U$  the interaction potential,  $\gamma = 6 \cdot 10^{-6}$  Ns/m the damping constant and  $R$   
664 the random force on the bead (see **Diffusion** above). To select a large damping constant that made simulations  
665 computationally efficient, we ran simulations where a single myosin molecule walked on a fixed actin  
666 filament and characterized the myosin load-free velocity with respect to the damping constant (SI  
667 Appendix/Fig. S16). A damping constant of  $\gamma = 6 \cdot 10^{-6}$  Ns/m was chosen to minimize computational cost  
668 without perturbing the myosin load-free velocity. Since we used the same damping constant for every bead in  
669 the system, the constant for a complex was proportional to the number of beads in the complex. Thus a small  
670 node of  $\sim 7$  unipolar myosins (having  $\sim 70$  beads) experienced a damping constant of  $\sim 420$  pNs/ $\mu\text{m}$ ,  
671 corresponding to a diffusion constant of  $\sim 10$  nm<sup>2</sup>/s, the experimental value reported by Vavylonis et al (15).  
672 Assuming the inertia of the bead was negligible, and thus  $M = 0$ , the displacement was simply a linear  
673 function of total force  $F$ :

$$dX = \frac{1}{\gamma} [-\nabla U(X) + R] dt = \frac{1}{\gamma} F dt$$

674 To prevent a large force from moving a bead too far, we constrained the maximal displacement of any bead in  
675 any time step (corresponding to the maximal force  $F_{max}$ ) to  $D_{max} = 0.01$  nm. Displacement  $D$  of each bead  
676 was then calculated as

$$D = \frac{D_{max}}{F_{max}} F$$

677 Since the time step was not a constant in our simulations, the average time step was calculated at the end of  
678 each simulation, which fell in the range of  $0.2 - 0.3$   $\mu$ s. Simulation codes were written in Fortran and the  
679 trajectories of each system were visualized using VMD (Visual Molecular Dynamics) (74).

680

### 681 **F-actin straightness**

682 To compare actin filament straightness in the tomograms and the simulations, we defined “straightness” as the  
683 filament’s contour length  $L_{contour}$  divided by the length of a straight line connecting the two ends  
684  $L_{end-to-end}$  (SI Appendix/Fig. S13E). Note that we did not compare persistence length, which is usually used  
685 to characterize free filaments not being pulled or acted upon by anything other than random thermal forces.

686

### 687 **Actin-membrane distance**

688 To compare the distances between the actin filaments and membranes in the tomograms and the simulations,  
689 we defined the distance from an actin bead to the membrane as the smallest distance from the actin bead to  
690 any membrane bead.

691

### 692 **Constriction rate**

693 For simplicity, the constriction rate was calculated as the inward growth of the cell wall,  $\Delta r / \Delta t$ , averaged  
694 around its circumference, where  $\Delta r$  was the radial displacement of the cell wall leading edge and  $\Delta t$  was the  
695 duration of constriction.

696

697 **Ring tension**

698 To calculate the ring tension during constriction, first the ring radius  $R_r$  was calculated as the average distance  
699 from the actin beads to the cell axis. The ring tension was then calculated as

$$T = \sum_i \frac{k_a(l_a^i - l_a)l_a^i \cos^2\theta_i}{2\pi R_r}$$

700 where the sum was over all actin springs  $i$  which had their length  $l_a^i$  larger than the relaxed length  $l_a$ ,  $k_a$  was  
701 the actin spring constant, and  $\theta_i$  was the angle spring  $i$  deviated from the circumferential direction.

702

703

## 704 **Experimental procedures**

### 705 **Microscopy**

706 Mid-log-phase cells were spotted on a 2% Agar pad supplemented with YES media and observed under a  
707 custom-built spinning disk confocal microscope with an inverted Olympus IX-83,100X/1.4 plan-apo  
708 objective, a deep cooled Hamamatsu ORCA II –ER CCD camera and Yokogawa CSU:X1 spinning disk  
709 (Perkin-Elmer). A stack of 18–20 Z slices of 0.3 mm Z-step-size was collected every 2 min for an hour at  
710 25°C using the Velocity software (Perkin-Elmer). Images were then rotated and cropped using the imageJ  
711 software to align cells and 3D reconstruction was done using the Velocity software.

712

### 713 **Fluorescence Recovery After Photobleaching (FRAP)**

714 Cells were mounted onto a 2% Agar pad supplemented with YES media and observed under a Leica TCS SP8  
715 scanning confocal microscope with a 63x magnification, 1.4 numerical aperture (NA) oil-immersion objective.  
716 The experiments were performed at 25°C unless otherwise indicated. For excitation of GFP, we used a 488 nm  
717 Argon laser. Images were collected with a scan speed of 40 fps, 12x digital zoom, at 256 x 256 pixels. The  
718 laser intensity for photobleaching was adjusted to obtain ~80% loss of fluorescence in the approximately 0.2  
719  $\mu\text{m} \times 0.2 \mu\text{m}$  circular bleached region of the cytokinetic ring. To allow rapid bleaching, we used a high laser  
720 intensity with 1–3 iterations of the bleaching scan. The images were collected before and after bleaching,  
721 using low laser intensities and FRAP was monitored for 1.5 to 2 min. Data from the experiment were analyzed  
722 using ImageJ (National Institute Of Health, Bethesda, MD) with FRAP plugin  
723 ([www.embl.de/eamnet/frap/FRAP6.html](http://www.embl.de/eamnet/frap/FRAP6.html)) using the double normalization method (75). Normalized curves  
724 were fitted to single exponential functions to extract the mobile fraction and half-life.

725

## 726 **Acknowledgments**

727 The authors thank Catherine Oikonomou for helping revise the manuscript for clarity. The work was  
728 supported in part by NIH grant R35 GM122588 to GJJ.

## 729 **References**

- 730 1. Balasubramanian MK, Bi E, Glotzer M (2004) Comparative analysis of cytokinesis in budding yeast,  
731 fission yeast and animal cells. *Curr Biol CB* 14(18):R806-818.
- 732 2. Pollard TD (2010) Mechanics of cytokinesis in eukaryotes. *Curr Opin Cell Biol* 22(1):50–56.
- 733 3. Geeves MA, Holmes KC (2005) The molecular mechanism of muscle contraction. *Adv Protein Chem*  
734 71:161–193.
- 735 4. Marks J, Hyams JS (1985) Localization of F-actin through the cell division cycle of  
736 *Schizosaccharomyces pombe*. *Eur J Cell Biol* 39(1):27–32.
- 737 5. Kanbe T, Kobayashi I, Tanaka K (1989) Dynamics of cytoplasmic organelles in the cell cycle of the  
738 fission yeast *Schizosaccharomyces pombe*: three-dimensional reconstruction from serial sections. *J*  
739 *Cell Sci* 94 ( Pt 4):647–656.
- 740 6. Kitayama C, Sugimoto A, Yamamoto M (1997) Type II myosin heavy chain encoded by the *myo2*  
741 gene composes the contractile ring during cytokinesis in *Schizosaccharomyces pombe*. *J Cell Biol*  
742 137(6):1309–1319.
- 743 7. Bezanilla M, Forsburg SL, Pollard TD (1997) Identification of a second myosin-II in  
744 *Schizosaccharomyces pombe*: *Myp2p* is conditionally required for cytokinesis. *Mol Biol Cell*  
745 8(12):2693–2705.
- 746 8. May KM, Watts FZ, Jones N, Hyams JS (1997) Type II myosin involved in cytokinesis in the fission  
747 yeast, *Schizosaccharomyces pombe*. *Cell Motil Cytoskeleton* 38(4):385–396.
- 748 9. Arai R, Nakano K, Mabuchi I (1998) Subcellular localization and possible function of actin,  
749 tropomyosin and actin-related protein 3 (*Arp3*) in the fission yeast *Schizosaccharomyces pombe*.  
750 *Eur J Cell Biol* 76(4):288–295.
- 751 10. Balasubramanian MK, et al. (1998) Isolation and characterization of new fission yeast cytokinesis  
752 mutants. *Genetics* 149(3):1265–1275.
- 753 11. Motegi F, Nakano K, Mabuchi I (2000) Molecular mechanism of myosin-II assembly at the division  
754 site in *Schizosaccharomyces pombe*. *J Cell Sci* 113 ( Pt 10):1813–1825.
- 755 12. Wu J-Q, Kuhn JR, Kovar DR, Pollard TD (2003) Spatial and temporal pathway for assembly and  
756 constriction of the contractile ring in fission yeast cytokinesis. *Dev Cell* 5(5):723–734.
- 757 13. Bähler J, et al. (1998) Role of polo kinase and *Mid1p* in determining the site of cell division in  
758 fission yeast. *J Cell Biol* 143(6):1603–1616.
- 759 14. Wu J-Q, et al. (2006) Assembly of the cytokinetic contractile ring from a broad band of nodes in  
760 fission yeast. *J Cell Biol* 174(3):391–402.
- 761 15. Vavylonis D, Wu J-Q, Hao S, O’Shaughnessy B, Pollard TD (2008) Assembly mechanism of the  
762 contractile ring for cytokinesis by fission yeast. *Science* 319(5859):97–100.

- 763 16. Swulius MT, et al. (2017) Structure of the fission yeast actomyosin ring during constriction.  
764 *bioRxiv*:194902.
- 765 17. Huang J, et al. (2012) Nonmedially assembled F-actin cables incorporate into the actomyosin ring  
766 in fission yeast. *J Cell Biol* 199(5):831–847.
- 767 18. Evangelista M, et al. (1997) Bni1p, a Yeast Formin Linking Cdc42p and the Actin Cytoskeleton  
768 During Polarized Morphogenesis. *Science* 276(5309):118–122.
- 769 19. Chang F, Drubin D, Nurse P (1997) cdc12p, a protein required for cytokinesis in fission yeast, is a  
770 component of the cell division ring and interacts with profilin. *J Cell Biol* 137(1):169–182.
- 771 20. Laporte D, Coffman VC, Lee I-J, Wu J-Q (2011) Assembly and architecture of precursor nodes  
772 during fission yeast cytokinesis. *J Cell Biol* 192(6):1005–1021.
- 773 21. May KM, Watts FZ, Jones N, Hyams JS (1997) Type II myosin involved in cytokinesis in the fission  
774 yeast, *Schizosaccharomyces pombe*. *Cell Motil Cytoskeleton* 38(4):385–396.
- 775 22. Laplante C, et al. (2015) Three Myosins Contribute Uniquely to the Assembly and Constriction of  
776 the Fission Yeast Cytokinetic Contractile Ring. *Curr Biol CB*. doi:10.1016/j.cub.2015.06.018.
- 777 23. Jung Y-W, Mascagni M (2014) Constriction model of actomyosin ring for cytokinesis by fission  
778 yeast using a two-state sliding filament mechanism. *J Chem Phys* 141(12):125101.
- 779 24. Stachowiak MR, et al. (2014) Mechanism of cytokinetic contractile ring constriction in fission yeast.  
780 *Dev Cell* 29(5):547–561.
- 781 25. Niederman R, Pollard TD (1975) Human platelet myosin. II. In vitro assembly and structure of  
782 myosin filaments. *J Cell Biol* 67(1):72–92.
- 783 26. Pollard TD (1982) Structure and polymerization of *Acanthamoeba* myosin-II filaments. *J Cell Biol*  
784 95(3):816–825.
- 785 27. Laplante C, Huang F, Tebbs IR, Bewersdorf J, Pollard TD (2016) Molecular organization of  
786 cytokinesis nodes and contractile rings by super-resolution fluorescence microscopy of live fission  
787 yeast. *Proc Natl Acad Sci* 113(40):E5876–E5885.
- 788 28. Skau CT, et al. (2011) Actin filament bundling by fimbrin is important for endocytosis, cytokinesis,  
789 and polarization in fission yeast. *J Biol Chem* 286(30):26964–26977.
- 790 29. Laporte D, Ojkic N, Vavylonis D, Wu J-Q (2012)  $\alpha$ -Actinin and fimbrin cooperate with myosin II to  
791 organize actomyosin bundles during contractile-ring assembly. *Mol Biol Cell* 23(16):3094–3110.
- 792 30. Wu JQ, Bähler J, Pringle JR (2001) Roles of a fimbrin and an alpha-actinin-like protein in fission  
793 yeast cell polarization and cytokinesis. *Mol Biol Cell* 12(4):1061–1077.
- 794 31. Mishra M, et al. (2013) In vitro contraction of cytokinetic ring depends on myosin II but not on  
795 actin dynamics. *Nat Cell Biol* 15(7):853–859.
- 796 32. Nakano K, Mabuchi I (2006) Actin-depolymerizing protein Adf1 is required for formation and  
797 maintenance of the contractile ring during cytokinesis in fission yeast. *Mol Biol Cell* 17(4):1933–  
798 1945.

- 799 33. Chen Q, Pollard TD (2011) Actin filament severing by cofilin is more important for assembly than  
800 constriction of the cytokinetic contractile ring. *J Cell Biol* 195(3):485–498.
- 801 34. Pollard TD (2014) The value of mechanistic biophysical information for systems-level  
802 understanding of complex biological processes such as cytokinesis. *Biophys J* 107(11):2499–2507.
- 803 35. Zumdieck A, Kruse K, Bringmann H, Hyman AA, Jülicher F (2007) Stress generation and filament  
804 turnover during actin ring constriction. *PLoS One* 2(8):e696.
- 805 36. Mendes Pinto I, Rubinstein B, Kucharavy A, Unruh JR, Li R (2012) Actin depolymerization drives  
806 actomyosin ring contraction during budding yeast cytokinesis. *Dev Cell* 22(6):1247–1260.
- 807 37. Bidone TC, Tang H, Vavylonis D (2014) Dynamic Network Morphology and Tension Buildup in a 3D  
808 Model of Cytokinetic Ring Assembly. *Biophys J* 107(11):2618–2628.
- 809 38. Galkin VE, Orlova A, Egelman EH (2012) Actin Filaments as Tension Sensors. *Curr Biol* 22(3):R96–  
810 R101.
- 811 39. Uyeda TQP, Iwadate Y, Umeki N, Nagasaki A, Yumura S (2011) Stretching Actin Filaments within  
812 Cells Enhances their Affinity for the Myosin II Motor Domain. *PLoS ONE* 6(10):e26200.
- 813 40. Hayakawa K, Tatsumi H, Sokabe M (2011) Actin filaments function as a tension sensor by tension-  
814 dependent binding of cofilin to the filament. *J Cell Biol* 195(5):721–727.
- 815 41. Pelham RJ, Chang F (2002) Actin dynamics in the contractile ring during cytokinesis in fission  
816 yeast. *Nature* 419(6902):82–86.
- 817 42. Clifford DM, et al. (2008) The Clp1/Cdc14 phosphatase contributes to the robustness of cytokinesis  
818 by association with anillin-related Mid1. *J Cell Biol* 181(1):79–88.
- 819 43. Pollard TD, Wu J-Q (2010) Understanding cytokinesis: lessons from fission yeast. *Nat Rev Mol Cell*  
820 *Biol* 11(2):149–155.
- 821 44. Zhou Z, et al. (2014) The contractile ring coordinates curvature dependent septum assembly  
822 during fission yeast cytokinesis. *Mol Biol Cell*. doi:10.1091/mbc.E14-10-1441.
- 823 45. Thiyagarajan S, Munteanu EL, Arasada R, Pollard TD, O’Shaughnessy B (2015) The fission yeast  
824 cytokinetic contractile ring regulates septum shape and closure. *J Cell Sci* 128(19):3672–3681.
- 825 46. Kruse K, Jülicher F (2000) Actively Contracting Bundles of Polar Filaments. *Phys Rev Lett*  
826 85(8):1778–1781.
- 827 47. Ennomani H, et al. (2016) Architecture and Connectivity Govern Actin Network Contractility. *Curr*  
828 *Biol* 26(5):616–626.
- 829 48. Bendix PM, et al. (2008) A Quantitative Analysis of Contractility in Active Cytoskeletal Protein  
830 Networks. *Biophys J* 94(8):3126–3136.
- 831 49. Dasanayake NL, Michalski PJ, Carlsson AE (2011) General Mechanism of Actomyosin Contractility.  
832 *Phys Rev Lett* 107(11):118101.

- 833 50. Lenz M (2014) Geometrical Origins of Contractility in Disordered Actomyosin Networks. *Phys Rev X*  
834 4(4):041002.
- 835 51. Padmanabhan A, et al. (2011) IQGAP-related Rng2p organizes cortical nodes and ensures position  
836 of cell division in fission yeast. *Curr Biol CB* 21(6):467–472.
- 837 52. McDonald NA, Lind AL, Smith SE, Li R, Gould KL (2017) Nanoscale architecture of the  
838 *Schizosaccharomyces pombe* contractile ring. *eLife* 6:e28865.
- 839 53. Dominguez R, Holmes KC (2011) Actin structure and function. *Annu Rev Biophys* 40:169–186.
- 840 54. Kojima H, Ishijima A, Yanagida T (1994) Direct measurement of stiffness of single actin filaments  
841 with and without tropomyosin by in vitro nanomanipulation. *Proc Natl Acad Sci U S A*  
842 91(26):12962.
- 843 55. Isambert H, et al. (1995) Flexibility of actin filaments derived from thermal fluctuations. Effect of  
844 bound nucleotide, phalloidin, and muscle regulatory proteins. *J Biol Chem* 270(19):11437–11444.
- 845 56. Bezanilla M, Pollard TD (2000) Myosin-II tails confer unique functions in *Schizosaccharomyces*  
846 *pombe*: characterization of a novel myosin-II tail. *Mol Biol Cell* 11(1):79–91.
- 847 57. Finer JT, Simmons RM, Spudich JA (1994) Single myosin molecule mechanics: piconewton forces  
848 and nanometre steps. *Nature* 368(6467):113–119.
- 849 58. De La Cruz EM, Ostap EM (2009) Kinetic and equilibrium analysis of the myosin ATPase. *Methods*  
850 *Enzymol* 455:157–192.
- 851 59. Heissler SM, Liu X, Korn ED, Sellers JR (2013) Kinetic Characterization of the ATPase and Actin-  
852 activated ATPase Activities of *Acanthamoeba castellanii* Myosin-2. *J Biol Chem* 288(37):26709–  
853 26720.
- 854 60. Lord M, Pollard TD (2004) UCS protein Rng3p activates actin filament gliding by fission yeast  
855 myosin-II. *J Cell Biol* 167(2):315–325.
- 856 61. Murphy ACH, Young PW (2015) The actinin family of actin cross-linking proteins – a genetic  
857 perspective. *Cell Biosci* 5. doi:10.1186/s13578-015-0029-7.
- 858 62. Claessens MMAE, Bathe M, Frey E, Bausch AR (2006) Actin-binding proteins sensitively mediate F-  
859 actin bundle stiffness. *Nat Mater* 5(9):748–753.
- 860 63. Xu J, Wirtz D, Pollard TD (1998) Dynamic cross-linking by alpha-actinin determines the mechanical  
861 properties of actin filament networks. *J Biol Chem* 273(16):9570–9576.
- 862 64. Li Y, et al. (2016) The F-actin bundler  $\alpha$ -actinin Ain1 is tailored for ring assembly and constriction  
863 during cytokinesis in fission yeast. *Mol Biol Cell*. doi:10.1091/mbc.E16-01-0010.
- 864 65. Bo L, Waugh RE (1989) Determination of bilayer membrane bending stiffness by tether formation  
865 from giant, thin-walled vesicles. *Biophys J* 55(3):509–517.
- 866 66. Proctor SA, Minc N, Boudaoud A, Chang F (2012) Contributions of Turgor Pressure, the Contractile  
867 Ring, and Septum Assembly to Forces in Cytokinesis in Fission Yeast. *Curr Biol* 22(17):1601–1608.

- 868 67. Box GEP, Muller ME (1958) A Note on the Generation of Random Normal Deviates. *Ann Math Stat*  
869 29(2):610–611.
- 870 68. Wu J-Q, Pollard TD (2005) Counting Cytokinesis Proteins Globally and Locally in Fission Yeast.  
871 *Science* 310(5746):310–314.
- 872 69. Dobbelaere J, Barral Y (2004) Spatial Coordination of Cytokinetic Events by Compartmentalization  
873 of the Cell Cortex. *Science* 305(5682):393–396.
- 874 70. Wloka C, et al. (2011) Evidence that a septin diffusion barrier is dispensable for cytokinesis in  
875 budding yeast. *Biol Chem* 392(8–9):813–829.
- 876 71. Berlin A, Paoletti A, Chang F (2003) Mid2p stabilizes septin rings during cytokinesis in fission  
877 yeast. *J Cell Biol* 160(7):1083–1092.
- 878 72. Tasto JJ, Morrell JL, Gould KL (2003) An anillin homologue, Mid2p, acts during fission yeast  
879 cytokinesis to organize the septin ring and promote cell separation. *J Cell Biol* 160(7):1093–1103.
- 880 73. McDonald NA, Vander Kooi CW, Ohi MD, Gould KL (2015) Oligomerization but Not Membrane  
881 Bending Underlies the Function of Certain F-BAR Proteins in Cell Motility and Cytokinesis. *Dev Cell*  
882 35(6):725–736.
- 883 74. Humphrey W, Dalke A, Schulten K (1996) VMD: Visual molecular dynamics. *J Mol Graph* 14(1):33–  
884 38.
- 885 75. Phair RD, Gorski SA, Misteli T (2004) Measurement of dynamic protein binding to chromatin in  
886 vivo, using photobleaching microscopy. *Methods Enzymol* 375:393–414.
- 887